# Modeling columnar thin films as platforms for surface–plasmonic–polaritonic optical sensing

Tom G. Mackay<sup>1</sup>

School of Mathematics and Maxwell Institute for Mathematical Sciences University of Edinburgh, Edinburgh EH9 3JZ, UK

and

NanoMM — Nanoengineered Metamaterials Group Department of Engineering Science and Mechanics Pennsylvania State University, University Park, PA 16802–6812, USA

Akhlesh Lakhtakia<sup>2</sup>

NanoMM — Nanoengineered Metamaterials Group Department of Engineering Science and Mechanics Pennsylvania State University, University Park, PA 16802–6812, USA

#### Abstract

Via exploitation of surface plasmon polaritons (SPPs), columnar thin films (CTFs) are attractive potential platforms for optical sensing as their relative permittivity dyadic and porosity can be tailored to order. Nanoscale model parameters of a CTF were determined from its measured relative permittivity dyadic, after inverting the Bruggeman homogenization formalism. These model parameters were then used to determine the relative permittivity dyadic of a fluid–infiltrated CTF. Two boundary–value problems were next solved: the first relating to SPP–wave propagation guided by the planar interface of a semi–infinitely thick metal and a semi–infinitely thick CTF, and the second to the plane–wave response of the planar interface of a finitely thick metallic layer and a CTF in a modified Kretschmann configuration. Numerical studies revealed that SPP waves propagate at a lower phase speed and with a shorter propagation length, if the fluid has a larger refractive index. Furthermore, the angle of incidence required to excite an SPP wave in a modified Kretschmann configuration increases as the refractive index of the fluid increases.

Keywords: Bruggeman homogenization formalism, surface plasmon polariton, columnar thin film

### 1 Introduction

Research on optical sensors exploiting surface plasmon polaritons (SPPs) has recorded an explosive growth [1, 2, 3] and commercial success [4, 5] during the last two decades. SPPs are virtual particles [6] that can propagate guided by the planar interface of a metal and a dielectric material, the classical analog of a train of SPPs being an SPP wave.

Although several different sensing configurations have been investigated to excite SPP waves, perhaps the most commonplace is the Kretschmann configuration [7]. Both the metal and its dielectric partner in this configuration are layers of finite thickness. The metal film's thickness is  $\sim 100$  nm, whereas the dielectric layer has to be much thicker. On the other side of the metal film is a dielectric coupling material (in the form

<sup>&</sup>lt;sup>1</sup>E-mail: T.Mackay@ed.ac.uk.

 $<sup>^2\</sup>mathrm{E-mail:}$ akhlesh@psu.edu

of a prism), which is optically denser than the dielectric material. Quasi-monochromatic light is launched at an angle to the thickness direction in the coupling material towards the metal film. The fraction of illuminating light that is neither reflected nor transmitted is absorbed. As the angle of incidence increases from 0 towards  $\pi/2$ , a sharp peak in absorbance, accompanied by minuscule reflectance and transmittance, indicates the excitation of an SPP wave. This sharp peak occurs only for *p*-polarized light, and its angular location shifts when the refractive index of the dielectric partnering layer is altered by the incorporation of an analyte.

The analyte can be incorporated in a variety of ways. One is to use a liquid such as water as the dielectric partner. Either the dispersal of the analyte in that liquid or the binding of the analyte to recognition molecules attached to the metal film can lead to an angular shift [2, 3]. Another way is to use a highly porous, thin metal film [8, 9], so that it can be infiltrated by an analyte-containing liquid [10, 11].

The dielectric partnering layer need not have an effectively isotropic constitution for the excitation of SPP waves. Uniaxial dielectric materials have been extensively considered for the role of the dielectric partnering material, both theoretically and experimentally [12, 13, 14, 15, 16]. Another class of candidates for this role is that of columnar thin films (CTFs), which are effectively biaxial dielectric materials [17].

A columnar thin film is an assembly of parallel nanowires, grown on a planar substrate by physical vapor deposition [17, 18]. As schematically illustrated in Fig. 1, the column inclination angle  $\chi \in (0, \pi/2]$  is equal to or greater than the vapor incidence angle  $\chi_v \in (0, \pi/2]$ . By control of the deposition-process parameters the vapor incidence angle in particular—and the material(s) evaporated, both the optical properties and the porosity of CTFs may be tailored to order, thereby controlling the excitation conditions for SPP waves [19, 20]. This renders CTFs attractive as potential platforms for optical sensing of chemical and/or biological species that may infiltrate the void regions of the CTF [21, 22].

Our aim for the study reported here was to determine the sensitivity of SPP-wave excitation at the planar interface of a metal and a CTF to changes in the refractive index of the fluid infiltrating the void regions of the CTF. Employing the relative permittivity dyadic of an uninfiltrated CTF, this study is largely numerical. It is primarily based on theoretical results established in two recent papers: one on the theory of exciting an SPP wave that propagates parallel to the morphologically significant plane of the CTF [19], the second on inverting the Bruggeman homogenization formalism with data on the uninfiltrated CTF [23] for use in a forward Bruggeman formalism [25] to compute the effective relative permittivity dyadic of the infiltrated CTF.

The plan of this paper is as follows: Section 2 succinctly describes the inverse and forward Bruggeman homogenization formalisms for the uninfiltrated and the infiltrated CTF. Two boundary–value problems are formulated and solved next:

- (i) The first is a canonical problem relating to SPP–wave propagation guided by the planar interface of a semi–infinitely thick metal and a semi–infinitely thick CTF (Sec. 3), and
- (ii) the second is a realistic problem involving the plane–wave response of the planar interface of a finitely thick metallic layer and a CTF in a modified Kretschmann configuration (Sec. 4).

Detailed descriptions of theoretical formulations are available in the predecessor papers [19, 23]. In the notation adopted,  $3\times3$  dyadics are double underlined while 3-vectors are in boldface; unit vectors along the Cartesian axes are denoted  $\mathbf{u}_x$ ,  $\mathbf{u}_y$  and  $\mathbf{u}_z$ . The operators Re [·] and Im [·] deliver the real and imaginary parts of complex-valued quantities; and  $i = \sqrt{-1}$ . The free-space wavenumber is  $k_0$  and the intrinsic impedance of free space is  $\eta_0$ . An  $\exp(-i\omega t)$  time-dependence is implicit, with  $\omega$  as the angular frequency and t as time.

## 2 Homogenization studies on CTFs

#### 2.1 Preliminaries

Let us begin with an uninfiltrated CTF characterized at length scales much greater than the nanoscale by the relative permittivity dyadic

$$\underline{\epsilon}_{ctf1} = \epsilon_{a1} \mathbf{u}_n \mathbf{u}_n + \epsilon_{b1} \mathbf{u}_\tau \mathbf{u}_\tau + \epsilon_{c1} \mathbf{u}_b \mathbf{u}_b.$$
(1)

Herein the normal, tangential and binormal basis vectors are specified in terms of the column inclination angle  $\chi \in (0, \pi/2]$  per

$$\mathbf{u}_{n} = -\mathbf{u}_{x} \sin \chi + \mathbf{u}_{z} \cos \chi \mathbf{u}_{\tau} = \mathbf{u}_{x} \cos \chi + \mathbf{u}_{z} \sin \chi \mathbf{u}_{b} = -\mathbf{u}_{y}$$
 (2)

The CTF is grown on a planar substrate, which we take to lie parallel to z = 0, through the deposition of an evaporated bulk material. The vapor incidence angle  $\chi_v$  is less than or equal to the column inclination angle  $\chi$ , as schematically illustrated in Fig. 1. The deposited material is assumed to be an isotropic dielectric material with refractive index  $n_s$ . The morphologically significant plane of the CTF is the xz plane [18, Chap. 7].

For the purposes of generating the numerical results presented in the following sections, we selected CTFs made from evaporating patinal<sup>®</sup> titanium oxide. The relative permittivity parameters of these CTFs are

$$\epsilon_{a1} = \left[ 1.0443 + 2.7394 \left( \frac{2\chi_v}{\pi} \right) - 1.3697 \left( \frac{2\chi_v}{\pi} \right)^2 \right]^2$$

$$\epsilon_{b1} = \left[ 1.6765 + 1.5649 \left( \frac{2\chi_v}{\pi} \right) - 0.7825 \left( \frac{2\chi_v}{\pi} \right)^2 \right]^2$$

$$\epsilon_{c1} = \left[ 1.3586 + 2.1109 \left( \frac{2\chi_v}{\pi} \right) - 1.0554 \left( \frac{2\chi_v}{\pi} \right)^2 \right]^2$$
(3)

with

$$\tan \chi = 2.8818 \tan \chi_v,\tag{4}$$

as determined by experimental measurements at a free–space wavelength of 633 nm [24].

Each column of a CTF can be modeled as an assembly of elongated ellipsoidal inclusions, strung together end-to-end [18, Chap. 6]. The inclusions have identical orientations and shapes. The inclusion surface is characterized by the dyadic

$$\mathbf{u}_n \, \mathbf{u}_n + \gamma_\tau \, \mathbf{u}_\tau \, \mathbf{u}_\tau + \gamma_b \, \mathbf{u}_b \, \mathbf{u}_b. \tag{5}$$

The highly aciculate nature of the columnar morphology suggests that the shape parameters  $\gamma_b \gtrsim 1$  and  $\gamma_\tau \gg 1$ . In fact, we fix  $\gamma_\tau = 15$  since increasing  $\gamma_\tau$  beyond 10 does not bring about significant effects for slender inclusions [25]. The CTF's columns occupy only a proportion  $f \in (0, 1)$  of the total CTF volume. The volume fraction of the CTF not occupied by columns is 1 - f.

#### 2.2 Inverse Bruggeman formalism — uninfiltrated CTF

While the relative-permittivity parameters  $\{\epsilon_{a1}, \epsilon_{b1}, \epsilon_{c1}\}$  may be straightforwardly measured, the same is not true for the nanoscale model parameters  $\{n_s, f, \gamma_b\}$ . The refractive index of the bulk material is known prior to evaporation, but the refractive index of the deposited material may be quite different, depending on the precise details of the deposition environment [26, 27, 28]. Also, the accurate determinations of  $\gamma_b$ from scanning-electron micrographs [17], and f by gas-adsorption techniques [29, 30, 31] or mass density measurements [26], are known to be problematic. Therefore, our first goal in this section is to establish the CTF nanoscale parameters  $\{n_s, f, \gamma_b\}$ , from a knowledge of the eigenvalues  $\{\epsilon_{a1}, \epsilon_{b1}, \epsilon_{c1}\}$  of  $\underline{\epsilon}_{ctf1}$ . The void regions of the uninfiltrated CTF are taken to be vacuous.

The computation of  $\{n_s, f, \gamma_b\}$  can be undertaken using the process of inverse homogenization. The widely used Bruggeman homogenization formalism [32, 33] provides an suitable framework for this process. Since we have recently described this inverse homogenization process in detail elsewhere [23], here we need only present the results.

For the titanium–oxide CTF described by the constitutive parameters (3) and (4), the corresponding values of  $\{n_s, f, \gamma_b\}$  are presented in Table 1 for  $\chi_v \in \{15^\circ, 30^\circ, 60^\circ, 90^\circ\}$ . The calculated data are in accord with previous observations:

- As  $\chi_v$  increases towards  $\pi/2$ , the biaxiality of a CTF reduces towards uniaxiality [17], which is reflected by the tendency of  $\gamma_b$  in Table 1 to reduce to almost unity.
- CTFs deposited more obliquely tend to have lower mass density [18, Chap. 5],[34]. This is confirmed Table 1 by the monotonic growth in the volume fraction f as  $\chi_v$  increases towards  $\pi/2$ .

We also noticed a steady decrease in  $n_s$  towards the bulk refractive index of titanium oxide, as  $\chi_v \to \pi/2$ . This trend does depend on the material deposited, and can even be turned into a steady increase [23]. It suggests the complexity of the roles played by the nanoscale parameters  $\{n_s, f, \gamma_b\}$  in the emergence of the relative–permittivity parameters  $\{\epsilon_{a1}, \epsilon_{b1}, \epsilon_{c1}\}$ .

#### 2.3 Forward homogenization — infiltrated CTF

In an optical sensor exploiting the SPP-wave phenomenon, the void regions of the CTF have to be filled with a fluid of refractive index  $n_{\ell}$ . As a result,  $\underline{\epsilon}_{ctf1}$  comprising the eigenvalues  $\{\epsilon_{a1}, \epsilon_{b1}, \epsilon_{c1}\}$  changes to  $\underline{\epsilon}_{ctf2}$  comprising new eigenvalues  $\{\epsilon_{a2}, \epsilon_{b2}, \epsilon_{c2}\}$ ; the column inclination angle  $\chi$  remains unchanged. From knowledge of the nanoscale model parameters  $\{n_s, f, \gamma_b\}$  as well as of  $\{n_{\ell}, \gamma_{\tau}\}$ , the Bruggeman homogenization formalism can be applied in its usual forward sense to determine  $\{\epsilon_{a2}, \epsilon_{b2}, \epsilon_{c2}\}$ . A description of the forward Bruggeman formalism as applied to a CTF is available elsewhere [25].

After using the nanoscale model parameters presented in Table 1, the corresponding values of  $\{\epsilon_{a2}, \epsilon_{b2}, \epsilon_{c2}\}$ were plotted against  $n_{\ell} \in (1.0, 1.5)$  in Fig. 2 for  $\chi_v \in \{15^{\circ}, 30^{\circ}, 60^{\circ}, 90^{\circ}\}$ . We see that each of  $\epsilon_{a2}, \epsilon_{b2}$  and  $\epsilon_{c2}$  increases approximately linearly as  $n_{\ell}$  increases. Also, the rate of increase is greater for smaller values of  $\chi_v$ , because the CTF is then more porous.

## 3 Canonical boundary–value problem

Let us now investigate the wavenumbers of SPP waves guided by the planar interface of two half–spaces, one filled with a metal and the other occupied by a CTF. Since the underlying theory for this canonical problem is described elsewhere [19], here we present only the key theoretical results as a precursor to our numerical results.

Suppose that the half-space z > 0 is occupied by a fluid-infiltrated CTF while a metal of relative permittivity  $\epsilon_m$  occupies the half-space z < 0. The SPP wave under consideration is *p*-polarized and propagates in the xz plane. In the metal half-space, the electromagnetic phasors are

$$\mathbf{E}(\mathbf{r}) = A_m \left( \mathbf{u}_x - \frac{i\sigma}{q_m} \mathbf{u}_z \right) \exp\left[ ik_0 \left( \sigma x - iq_m z \right) \right] \\
\mathbf{H}(\mathbf{r}) = A_m \frac{i\epsilon_m}{\eta_0 q_m} \mathbf{u}_y \exp\left[ ik_0 \left( \sigma x - iq_m z \right) \right] \\$$
(6)

where  $A_m$  is the complex-valued amplitude,  $q_m = \sqrt{\sigma^2 - \epsilon_m}$  and  $\sigma k_0 \mathbf{u}_x$  represents the wave vector of the SPP wave. By choosing Re  $[q_m] > 0$ , we ensure that this wave decays away from the interface z = 0. The

corresponding electromagnetic field phasors in the fluid-infiltrated-CTF half-space are

$$\mathbf{E}(\mathbf{r}) = A_c \left[ \mathbf{u}_x + \frac{i\sigma q_c - (\epsilon_{a2} - \epsilon_{b2})\sin\chi\cos\chi}{\sigma^2 - (\epsilon_{a2}\cos^2\chi + \epsilon_{b2}\sin^2\chi)} \mathbf{u}_z \right] \exp\left[ik_0\left(\sigma x + iq_c z\right)\right] \\
\mathbf{H}(\mathbf{r}) = A_c \frac{\sigma\left(\epsilon_{a2} - \epsilon_{b2}\right)\sin\chi\cos\chi - iq_c\left(\epsilon_{a2}\cos^2\chi + \epsilon_{b2}\sin^2\chi\right)}{\eta_0\left[\sigma^2 - \left(\epsilon_{a2}\cos^2\chi + \epsilon_{b2}\sin^2\chi\right)\right]} \mathbf{u}_y \exp\left[ik_0\left(\sigma x + iq_c z\right)\right] \\$$
(7)

where  $A_c$  is the complex-valued amplitude and the quadratic equation [19]

$$q_c^2 \left(\epsilon_{a2} \cos^2 \chi + \epsilon_{b2} \sin^2 \chi\right) + 2i\sigma q_c \left(\epsilon_{a2} - \epsilon_{b2}\right) \sin \chi \cos \chi - \sigma^2 \left(\epsilon_{a2} \sin^2 \chi + \epsilon_{b2} \cos^2 \chi\right) + \epsilon_{a2} \epsilon_{b2} = 0$$
(8)

yields  $q_c$ . The choice Re  $[q_c] > 0$  ensures that this wave decays away from the interface.

Upon applying the standard boundary conditions at z = 0, the dispersion relation [19]

$$\epsilon_m \sigma^2 + i q_m \sigma \left(\epsilon_{a2} - \epsilon_{b2}\right) \sin \chi \, \cos \chi + \left(q_m q_c - \epsilon_m\right) \left(\epsilon_{a2} \cos^2 \chi + \epsilon_{b2} \sin^2 \chi\right) = 0 \tag{9}$$

emerges, from which the relative wavenumber  $\sigma$  may be extracted by numerical means.

For illustrative purposes, let us choose the metal occupying z < 0 to be bulk aluminum, for which  $\epsilon_m = -56 + 21i$  at a free–space wavelength of 633 nm. In Fig. 3, the real and imaginary parts of  $\sigma$  are plotted against  $n_\ell$  for  $\chi_v \in \{15^\circ, 30^\circ, 60^\circ, 90^\circ\}$ . The real part of  $\sigma$  increases approximately linearly as  $n_\ell$  increases, and it also increases as  $\chi_v$  increases. From this we infer that the phase speed of the SPP wave decreases as  $n_\ell$  increases and as  $\chi_v$  increases. Similarly, the imaginary part of  $\sigma$  also increases as both  $n_\ell$  and  $\chi_v$  increase, and from this we infer that the attenuation of the SPP wave increases as  $n_\ell$  increases and as  $\chi_v$  increases.

## 4 Modified Kretschmann configuration

We now turn to a realistic setup for launching SPP waves along the planar interface of a metal film and a CTF of finite thickness. We examine a modification [19] of the Kretschmann configuration [7] wherein the regions  $z \leq 0$  and  $z \geq L_{\Sigma}$  are occupied by homogeneous, isotropic, nondissipative, dielectric materials with relative permittivity scalars  $\epsilon_d$  and  $\epsilon_\ell = n_\ell^2$ , respectively. The fluid–infiltrated CTF occupies the laminar region  $L_m \leq z \leq L_{\Sigma}$ , while the laminar region  $0 \leq z \leq L_m$  is occupied by a metal with relative permittivity  $\epsilon_m$ . A schematic representation of this modified Kretschmann configuration is provided in Fig. 4.

Let us consider a *p*-polarized plane wave in the region  $z \leq 0$ , propagating towards the metal-coated CTF at an angle  $\theta_{inc} \in (0, \pi/2)$  to the *z* axis, as described by the electromagnetic field phasors

$$\mathbf{E}_{inc} = (-\mathbf{u}_x \cos \theta_{inc} + \mathbf{u}_z \sin \theta_{inc}) \exp\left[i\left(\kappa x + \sqrt{\epsilon_d} z \cos \theta_{inc}\right)\right] \\ \mathbf{H}_{inc} = -\frac{\sqrt{\epsilon_d}}{\eta_0} \mathbf{u}_y \exp\left[i\left(\kappa x + \sqrt{\epsilon_d} z \cos \theta_{inc}\right)\right] \\ \right\}, \qquad z \le 0,$$
(10)

with

$$\kappa = k_0 \sqrt{\epsilon_d} \sin \theta_{inc}. \tag{11}$$

The corresponding reflected and transmitted electromagnetic field phasors are given as

$$\mathbf{E}_{ref} = r_p \left( \mathbf{u}_x \cos \theta_{inc} + \mathbf{u}_z \sin \theta_{inc} \right) \exp \left[ i \left( \kappa x - \sqrt{\epsilon_d} z \cos \theta_{inc} \right) \right] \\
\mathbf{H}_{ref} = -\frac{r_p \sqrt{\epsilon_d}}{\eta_0} \mathbf{u}_y \exp \left[ i \left( \kappa x - \sqrt{\epsilon_d} z \cos \theta_{inc} \right) \right] \\$$
(12)

and

$$\mathbf{E}_{tr} = t_p \left( -\mathbf{u}_x \cos \theta_{tr} + \mathbf{u}_z \sin \theta_{tr} \right) \exp \left[ i \left( \kappa x + \sqrt{\epsilon_\ell} \left( z - L_\Sigma \right) \cos \theta_{tr} \right) \right]$$

$$\mathbf{H}_{tr} = -\frac{t_p \sqrt{\epsilon_\ell}}{\eta_0} \mathbf{u}_y \exp \left[ i \left( \kappa x + \sqrt{\epsilon_\ell} \left( z - L_\Sigma \right) \cos \theta_{tr} \right) \right]$$

$$\left. \right\}, \qquad z \ge L_\Sigma, \qquad (13)$$

respectively, where

$$\sqrt{\epsilon_d} \sin \theta_{inc} = \sqrt{\epsilon_\ell} \sin \theta_{tr} = \sigma. \tag{14}$$

The complex-valued reflection and transmission coefficients, namely  $r_p$  and  $t_p$ , are determined by solving the related boundary-value problem. For full details, the reader is referred elsewhere [18, 19].

In studying surface waves at the metal-CTF interface, a key parameter is the absorbance

$$A_p = 1 - \left( |r_p|^2 + \frac{\sqrt{\epsilon_\ell} \operatorname{Re}\left[\cos\theta_{tr}\right]}{\sqrt{\epsilon_d}\cos\theta_{inc}} |t_p|^2 \right).$$
(15)

A characteristic signature of SPP–wave excitation is a peak in graph of  $A_p$  versus  $\theta_{inc}$ , when the angle of incidence exceeds the critical angle in the absence of the metal film.

For our numerical study, we chose  $L_m = 10$  nm and  $L_{\Sigma} = L_m + 1000$  nm. The existence of a critical angle for total reflection in the absence of the metal film follows by setting the relative permittivity  $\epsilon_d = 2.6^2 = 6.76$ , in the neighborhood of that which can be delivered by a rutile prism. In contrast, the relative permittivity  $\epsilon_\ell$  was kept variable. As in Sec. 3, aluminum was chosen as the metal.

In Fig. 5, graphs of  $A_p$  versus  $\theta_{inc}$  are presented for  $n_{\ell} \in \{1.0, 1.25, 1.5\}$  with  $\chi_v = 30^{\circ}$ . Also plotted versus  $\theta_{inc}$  is the quantity  $|r_p|^2$ , computed when  $L_m = 0$ ; these plots exhibit an abrupt step from 0 to 1, which occurs at the critical value of  $\theta_{inc}$  for total reflection. The rightmost peak in the graphs  $A_p$ , which occurs beyond the critical angle, indicates the excitation of SPP waves.

The fairly sharp spikes in the graphs of  $A_p$ , to the left of the rightmost peak, indicate bulk guided modes [35]. The  $\theta_{inc}$  values which correspond to these modes depend upon the thickness of the CTF. To demonstrate this, the plots of Fig. 5 are reproduced in Fig. 6 but with  $L_{\Sigma} = L_m + 1500$  nm. From a comparison of Figs. 5 and 6, it is clear that bulk guided modes for  $L_{\Sigma} = L_m + 1500$  nm arise at values of  $\theta_{inc}$  which are different to those for  $L_{\Sigma} = L_m + 1000$  nm. Importantly, the values of  $\theta_{inc}$  which correspond to the excitation of SPPs are the same for  $L_{\Sigma} = L_m + 1500$  nm and  $L_{\Sigma} = L_m + 1000$  nm.

The value of  $\theta_{inc}$  which corresponds to the rightmost peak in the graph of  $A_p$  — let us call this value  $\theta_{inc}^{\sharp}(n_{\ell})$  at a specified value of  $n_{\ell}$  — is clearly sensitive to both  $n_{\ell}$  and  $\chi_v$ . The value  $\theta_{inc}^{\sharp}(n_{\ell})$  increases as  $n_{\ell}$  increases and as  $\chi_v$  increases. In order to quantify the sensitivity of  $\theta_{inc}^{\sharp}(n_{\ell})$ , we introduce the figure of merit

$$\rho = \frac{\theta_{inc}^{\sharp}(n_{\ell}) - \theta_{inc}^{\sharp}(1.0)}{n_{\ell} - 1.0},\tag{16}$$

for  $n_{\ell} \in (1.0, 1.5)$ . Graphs of  $\rho$  versus  $n_{\ell}$  are provided in Fig. 7 for  $\chi_v \in \{15^\circ, 30^\circ, 60^\circ, 90^\circ\}$  and  $L_{\Sigma} = L_m + 1000$  nm. These clearly indicate that the metal–coated CTF can function as an optical sensor for an analyte dispersed uniformly in a solution. Furthermore, we observe that  $\theta_{inc}^{\sharp}(n_{\ell})$  is most sensitive to changes in  $n_{\ell}$  when  $\chi_v$  is small and  $n_{\ell}$  is large.

## 5 Closing remarks

Our numerical study has demonstrated that the excitation of an SPP wave guided by a planar interface of a metal films and a CTF is highly sensitive to the refractive index of a fluid infiltrating the CTF, as well as the morphology of the CTF itself. In particular, as the refractive index of the fluid increases, the phase speed of the SPP wave decreases and its degree of attenuation increases. Furthermore, the angle of incidence required to excite the SPP wave in a modified Kretschmann configuration increases as the refractive index of the fluid increases. This sensitivity bodes well for the implementation of fluid–infiltrated CTFs, as well as fluid–infiltrated sculptured thin films [18] more generally, as SPP–based optical sensors.

Acknowledgments: TGM is supported by a Royal Academy of Engineering/Leverhulme Trust Senior Research Fellowship. AL thanks the Binder Endowment at Penn State for partial financial support of his research activities.

## References

- R.J. Green, R.A. Frazier, K.M. Shakesheff, M.C. Davies, C.J. Roberts, S.J.B. Tendler, Surface plasmon resonance analysis of dynamic biological interactions with biomaterials, Biomater. 21 (2000) 1823–1835.
- [2] J. Homola, Present and future of surface plasmon resonance biosensors, Anal. Bioanal. Chem. 377 (2003) 528-539.
- [3] I. Abdulhalim, M. Zourob, A. Lakhtakia, Surface plasmon resonance for biosensing: A mini-review, Electromagnetics 28 (2008) 214-242.
- [4] S.K. Arya, A. Chaubey, B.D. Malhotra, Fundamentals and applications of biosensors, Proc. Ind. Nat. Acad. Sci. 72 (2006) 249–266.
- [5] J.H.T. Luong, K.B. Male, J.D. Glennon, Biosensor technology: Technology push versus market pull, Biotechnol. Adv. 26 (2008) 492–500.
- [6] D. Felbacq, Plasmons go quantum, J. Nanophoton. 2 (2008) 020302.
- [7] E. Kretschmann, H. Raether, Radiative decay of nonradiative surface plasmons excited by light, Z. Naturforsch. A 23 (1968) 2135–2136.
- [8] F. Yang, G.W. Bradberry, J.R. Sambles, The study of the optical properties of obliquely evaporated nickel films using IR surface plasmons, Thin Solid Films 196 (1991) 35–46.
- [9] A.I. Maaroof, A. Gentle, G.B. Smith, M.B. Cortie, Bulk and surface plasmons in highly nanoporous gold films, J. Phys. D: Appl. Phys. 40 (2007) 5675–5682.
- [10] I. Abdulhalim, A. Lakhtakia, A. Lahav, F. Zhang, J. Xu, Porosity effect on surface plasmon resonance from metallic sculptured thin films, Proc. SPIE 7041 (2008) 70410C.
- [11] A. Shalabney, A. Lakhtakia, I. Abdulhalim, A. Lahav, C. Patzig, I. Hazek, A. Karabchevsky, B. Rauschenbach, F. Zhang, J. Xu, Surface plasmon resonance from metallic columnar thin films, Photon. Nanostruct. Funda. Appli. (doi:10.1016/j.photonics.2009.03.003).
- [12] G.J. Sprokel, The reflectivity of a liquid crystal cell in a surface plasmon experiment, Mol. Cryst. Liq. Cryst. 68 (1981) 39–45.
- [13] G.J. Sprokel, R. Santo, J.D. Swalen, Determination of the surface tilt angle by attenuated total reflection, Mol. Cryst. Liq. Cryst. 68 (1981) 29–38.
- [14] J.P. Lloyd, C. Pearson, M.C. Petty, Surface plasmon resonance studies of gas effects in phthalocyanine Langmuir–Blodgett films, Thin Solid Films 160 (1988) 431–443.
- [15] H. Kano, W. Knoll, Locally excited surface-plasmon-polaritons for thickness measurement of LBK films, Opt. Commun. 153 (1998) 235–239.
- [16] A. Baba, F. Kaneko, K. Shinbo, K. Kato, S. Kobayashi, Evaluation of liquid crystal molecules on polyimide LB films using attenuated total reflection measurement, Thin Solid Films 327-329 (1998) 353–356.
- [17] I.J. Hodgkinson, Q.H. Wu, Birefringent Thin Films and Polarizing Elements, World Scientific, Singapore, 1998.
- [18] A. Lakhtakia, R. Messier, Sculptured Thin Films: Nanoengineered Morphology and Optics, SPIE Press, Bellingham, WA, USA, 2005.

- [19] A. Lakhtakia, J.A. Polo Jr., Morphological influence on surface–wave propagation at the planar interface of a metal film and a columnar thin film, Asian J. Phys. 17 (2008) 185–191. (The value of Im  $[\varkappa]$  for  $\chi_v = 5^\circ$  presented in Table 1 should be 0.0108.)
- [20] J.A. Polo Jr., A. Lakhtakia, Morphological effects on surface-plasmon-polariton waves at the planar interface of a metal and a columnar thin film, Opt. Commun. 281 (2008) 5453–5457.
- [21] D. Barreca, A. Gasparotto, C. Maccato, C. Maragno, E. Tondello, E. Comini, G. Sberveglieri, Columnar CeO<sub>2</sub> nanostructures for sensor application, Nanotechnology 18 (2007) 125502.
- [22] S.M. Pursel, M.W. Horn, Prospects for nanowire sculptured-thin-film devices, J. Vac. Sci. Technol. B 25 (2007) 2611–2615.
- [23] T.G. Mackay, A. Lakhtakia, Determination of constitutive and morphological parameters of columnar thin films by inverse homogenization, http://arxiv.org/abs/0909.5375
- [24] I. Hodgkinson, Q.h. Wu, J. Hazel, Empirical equations for the principal refractive indices and column angle of obliquely deposited films of tantalum oxide, titanium oxide, and zirconium oxide, Appl. Opt. 37 (1998) 2653–2659.
- [25] A. Lakhtakia, Enhancement of optical activity of chiral sculptured thin films by suitable infiltration of void regions, Optik 112 (2001) 145–148; corrections: 112 (2001) 544.
- [26] R. Messier, T. Takamori, R. Roy, Structure-composition variation in rf-sputtered films of Ge caused by process parameter changes, J. Vac. Sci. Technol. 13 (1976) 1060–1065.
- [27] J.R. Blanco, P.J. McMarr, J.E. Yehoda, K. Vedam, R. Messier, Density of amorphous germanium films by spectroscopic ellipsometry, J. Vac. Sci. Technol. A 4 (1986) 577–582.
- [28] F. Walbel, E. Ritter, R. Linsbod, Properties of TiO<sub>x</sub> films prepared by electron-beam evaporation of titanium and titanium suboxides, Appl. Opt. 42 (2003) 4590–4593.
- [29] S. Brunauer, P.H. Emmett, E. Teller, Adsorption of gases in multimolecular layers, J. Am. Chem. Soc. 60 (1938) 309–319.
- [30] G. Bomchil, R. Herino, K. Barla, J.C. Pfister, Pore size distribution in porous silicon studied by adsorption isotherms, J. Electrochem. Soc. 130 (1983) 1611–1614.
- [31] J.V. Ryan, M. Horn, A. Lakhtakia, C.G. Pantano, Characterization of sculptured thin films, Proc. SPIE 5593 (2004) 643–649.
- [32] W.S. Weiglhofer, A. Lakhtakia, B. Michel, Maxwell Garnett and Bruggeman formalisms for a particulate composite with bianisotropic host medium, Microwave Opt. Technol. Lett. 15 (1997) 263–266; corrections: 22 (1999) 221.
- [33] T.G. Mackay, A. Lakhtakia, Electromagnetic Anisotropy and Bianisotropy: A Field Guide, Word Scientific, Singapore, 2009.
- [34] R.N. Tait, T. Smy, M.J. Brett, Modelling and characterization of columnar growth in evaporated films, Thin Solid Films 226 (1993) 196–201.
- [35] K.R. Welford, J.R. Sambles, M.G. Clark, Guided modes and surface plasmon-polaritons observed with a nematic liquid crystal using attenuated total reflection, Liq. Cryst. 2 (1987) 91–105.

$\chi_v$	$\gamma_b$	f	$n_s$
$15^{\circ}$	2.2793	0.3614	3.2510
30°	1.8381	0.5039	3.0517
60°	1.4054	0.6956	2.9105
90°	1.0020	0.7859	2.8228

Table 1: The dimensionless quantities  $\gamma_b$ , f and  $n_s$  computed using the inverse Bruggeman homogenization formalism for a titanium–oxide CTF with  $\chi_v = 15^\circ$ ,  $30^\circ$ ,  $60^\circ$  and  $90^\circ$ .

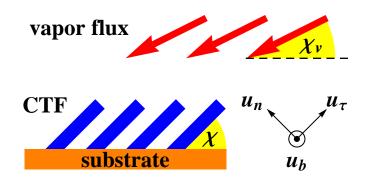


Figure 1: A columnar thin film growing with column inclination angle  $\chi$ , with the vapor incidence angle  $\chi_v \leq \chi$ . The columns grow along the direction of the unit vector  $\mathbf{u}_{\tau}$ .

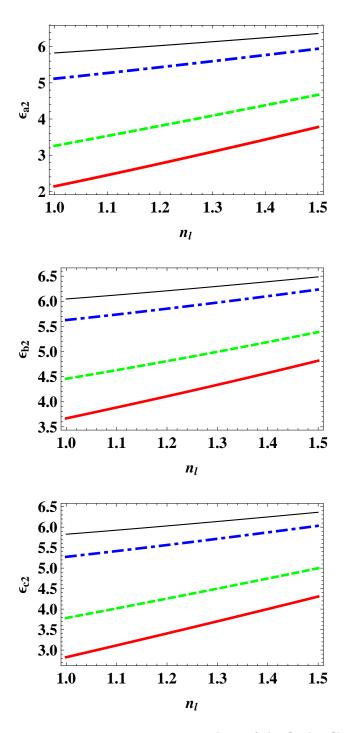


Figure 2: The relative permittivity-parameters  $\epsilon_{a2}$ ,  $\epsilon_{b2}$  and  $\epsilon_{c2}$  of the fluid-infiltrated CTF, as computed using the forward Bruggeman homgenization formalism, plotted against the refractive index  $n_{\ell}$  of the fluid infiltrating the void regions of the CTF, for  $\chi_v = 15^{\circ}$  (red, thick solid curve),  $30^{\circ}$  (green, dashed curve),  $60^{\circ}$ (blue, broken dashed curve) and  $90^{\circ}$  (black, thin solid curve).

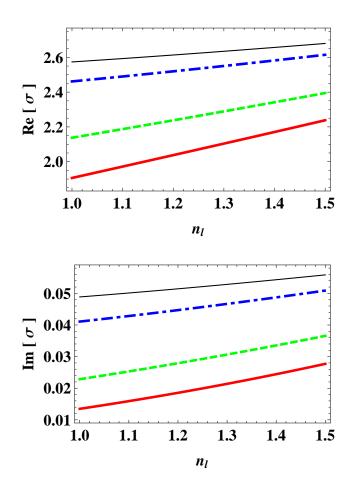


Figure 3: The real and imaginary parts of  $\sigma$  plotted against the refractive index  $n_{\ell}$  of the fluid infiltrating the void regions of the CTF for  $\chi_v = 15^{\circ}$  (red, thick solid curve),  $30^{\circ}$  (green, dashed curve),  $60^{\circ}$  (blue, broken dashed curve) and  $90^{\circ}$  (black, thin solid curve).

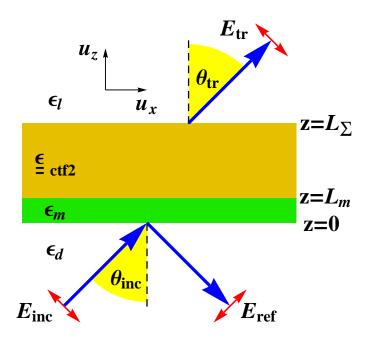


Figure 4: A p-polarized plane wave incident on a metal–coated CTF in the modified Kretschmann configuration.

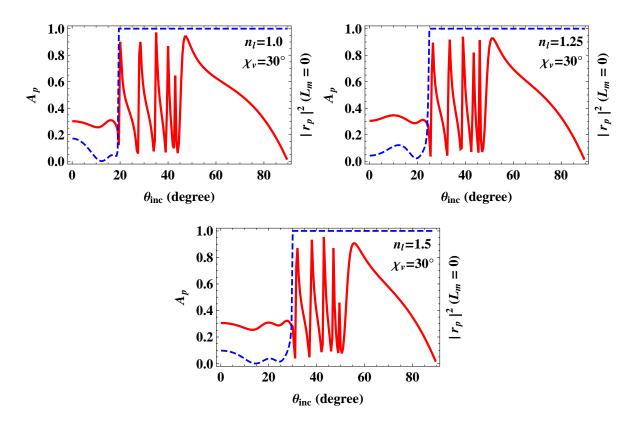


Figure 5: The absorbance  $A_p$  (red, solid curve) plotted against  $\theta_{inc}$  (in degree), when  $\epsilon_d = 9$ ,  $\epsilon_m = -56 + 21i$ ,  $L_m = 10$  nm,  $L_{\Sigma} = L_m + 1000$  nm,  $\chi_v = 30^{\circ}$  and  $n_{\ell} \in \{1.0, 1.25, 1.5\}$ . Also plotted is the quantity  $|r_p|^2$  (blue, dashed curve), calculated when  $L_m = 0$ .

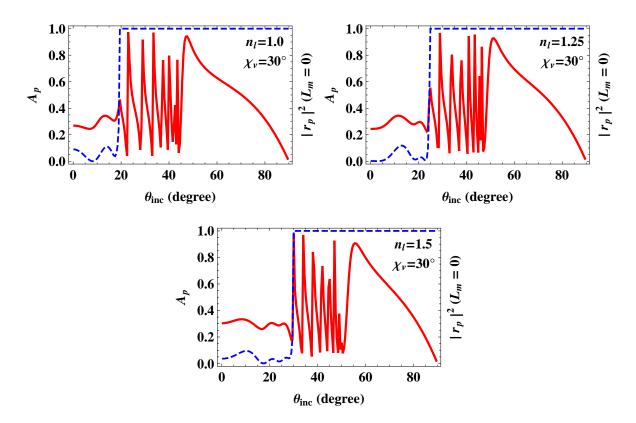


Figure 6: As Fig. 5 but with  $L_{\Sigma} = L_m + 1500$  nm.

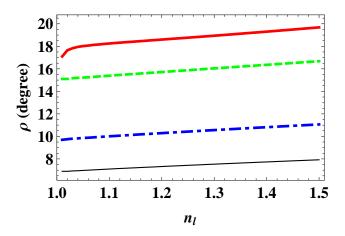


Figure 7: The figure of merit  $\rho$  (in degree) plotted against  $n_{\ell} \in (1.0, 1.5)$  for  $L_{\Sigma} = L_m + 1000$  nm with  $\chi_v = 15^{\circ}$  (red, thick solid curve), 30° (green, dashed curve), 60° (blue, broken dashed curve) and 90° (black, thin solid curve).